https://doi.org/10.5194/egusphere-2025-2687
Preprint. Discussion started: 27 August 2025

Kalman filter inversions on NO_x and VOCs emissions in China using TROPOMI satellite observations

Xiaohui Du[1,2], Wei Tang[2*], Chao Yu[3], Jing He[4], Zhongzhi Zhang[1], Yang Yu[1], Yang Li[1], Miaomiao Cheng[1], Fan Meng[5]

[1] Atmospheric Environment Institute, Chinese Research Academy of Environmental Sciences, Beijing 100012, China.
[2] State Key Laboratory of Environmental Criteria and Risk Assessment, Chinese Research Academy of Environmental Sciences, Beijing 100012, China.
[3] State Key Laboratory of Remote Sensing Science and Digital Earh, Aerospace Information Research Institute, Chinese Academy of Sciences. Beijing 100101, China.
[4] Xinjiang Institute of Environmental Protection Science, Urumqi 830000, China.
[5] Asia Center for Air Pollution Research, Nishi-ku, Niigata-shi, 9502144, Japan.

Correspondence to: Wei Tang (tangwei@craes.org.cn)

Abstract: Kalman filter inversions with multipollutant may improve the accuracy of inversion results and model performance. A joint inversion of VOCs and NO_x emissions was conducted using the HCHO and NO_2 column data from the TROPOspheric Monitoring Instrument and the simulated sensitivities of VOCs and NO_x from an air quality model from June to September 2019. The results showed that joint inversion results typically outperformed that of separate inversion in reducing model bias and error and regional variations of emission estimates under satellite data constraints. The inversed NO_x emissions over China decreased from a priori by approximately 30%, and the inversed VOCs emissions over China increased from a priori by around 50%. Joint inversion results aligned more closely with satellite-observed NO_2 and HCHO columns, capturing the unique belt-like distribution of HCHO and stabilizing maximum NO_2 column at approximately 15molec/cm². The accuracy of simulated ground-level ozone concentrations was enhanced by the joint inversion, with the mean bias decreased by 11.6μg/m³ overall. Meanwhile, ozone sensitivities prevalently shifted towards NO_x-limited conditions during summer after the joint inversion.

Keywords: Ozone modeling, Decoupled direct method, Kalman filter inversion, Satellite data, VOCs and NO_x emissions

https://doi.org/10.5194/egusphere-2025-2687
Preprint. Discussion started: 27 August 2025

1. Introduction

Tropospheric ozone (O_3), a secondary pollutant, is formed mainly through complex nonlinear photochemical reactions between NO_x and VOCs in sunlight. Investigating the nonlinear formation of O_3 and its precursors is complex and difficult. Since 1990s, countries in Europe and North America have adopted scientific emission control measures for the O_3 precursors (NO_x and VOCs), resulting in significant decrease in the levels of O_3 concentration (Jiang et al., 2020). Meanwhile, O_3 precursor emissions from anthropogenic sources have increased significantly in Asia, particularly in China, along with accelerated urbanization and industrialization. The maximum daily 8h O_3 concentration in summer has gradually increased, with an average growth rate of up to 3.73μg/m^3 per year in China overall from 2013−2019 (Li et al., 2020). The Chinese government has implemented various control measures to reduce NO_x and VOC emissions in alleviating O_3 pollution. With stringent emission control policies, the total amount of NO_x and VOC emissions from various sectors of anthropogenic sources in China were reduced significantly every year, which changes O_3 control strategies simultaneously. Hence, it is important to have a refined, accurate, and responsive anthropogenic emission inventory.

Earlier Chinese emission inventories were derived from a bottom-up statistical approach with continually updated local emission data. However, NO_x emissions have a relatively short lifetime and react quickly in the atmosphere, and the bottom-up inventories are mostly overestimated, even by a factor of approximately 2, compared to monitored or satellite-observed NO2 data (Silver et al., 2020). In addition, there is also significant uncertainty occurred in the estimates of VOCs emissions, leading to inaccurate modeling of O_3 concentrations (Lu et al., 2023). Furthermore, the bottom-up inventories rely on estimated emission activities to infer the spatial distribution, which can also generate significant uncertainties.

A top-down approach is an alternative way to estimate emissions based on observed air pollutant concentrations and source characteristics, and can be scientifically and objectively validated and improved through in situ observations, satellite data, and inverse modeling. Inverse modeling is a mathematical method has been widely used to estimate emission inventory by minimizing the difference between modeled and observed concentrations (Trombetti et al., 2018). As early as the mid-1960s, meteorologists applied the least squares method as a basic principle to construct atmospheric inversion models to reduce the bias between models and observations (Smagorjnsky, 1983). Martin et al. (2003) used a mass balance approach to invert regional NO_x emission intensities in conjunction with changes in NO_2 column concentrations from satellite data. However, since nonlinearity between NO_x emissions and NO_2 concentrations, this inversion method might underestimate NO_x emissions.

Many studies have been using various inversion methods to estimate emission inventories in combination with highly spatially covered satellite observations. Gerbig et al. (2003) and Khattatov et al. (1999) conducted Bayesian-based

https://doi.org/10.5194/egusphere-2025-2687
Preprint. Discussion started: 27 August 2025

estimation of emission inventories using satellite data and simulated pollutant sensitivities. Müller en Stavrakou, (2005) proposed a method that can invert multiple chemical species simultaneously, considering the interactions between chemical species as one of interacted pollutant undergo changes. Jung et al. (2022), Souri et al. (2020), and Wang et al. (2020) conducted several studies on joint inversion of multiple species such as NO_x and VOCs, SO_2 and NO_x, and CO and NO_x emissions. However, the Jacobian matrix settings in previous studies incorporated only the sensitivities of multiple pollutant concentrations to self-emissions during inversion process, without considering the cross-sensitivities of species interactions. It is important to include interspecies interactions from chemical transport models to deal with the nonlinear relationships in the iterative inversions.

The selection of NO_x and VOCs as focal precursors in this study is driven by their dominant roles in near-surface O_3 formation over China. While TROPOspheric monitoring instrument (TROPOMI) provides observations for multiple ozone precursors (e.g., CO with lower retrieval uncertainty), NO_2 and HCHO offer superior diagnostic value for local emission adjustments due to their short atmospheric lifetimes (hours to days) and direct participation in rapid photochemical O_3 production. In contrast, CO (lifetime ~2 months) influences O_3 indirectly through atmospheric oxidation capacity modulation, exhibiting lagged and nonlinear effects.

The uncertainties in VOCs and NO_x emission inventory in China pose a challenge for achieving relatively accurate predictions of O_3 levels. In this study, a discrete Kalman filter (DKF) inversion method of Tang et al. (2013) combined with the European TROPOMI satellite HCHO and NO_2 data was used to generate a top-down VOCs and NO_x emission inventory. The cross-sensitivities of NO_2 and HCHO concentrations to NO_x and VOC emissions computed by the Comprehensive Air Quality Model with Extensions (CAMx v7.10)-decoupled direct method (DDM) were also incorporated into the inversion framework. The joint DKF inversions allowed us quantify NO_x and VOCs emissions simultaneously, providing more accurately O_3 precursor emissions to simulate the O_3 formation and its control strategy.

2. Inverse modeling method and materials

2.1 TROPOMI NO_2 and HCHO column retrievals

TROPOMI on the Sentinel-5 precursor, launched in October 2017, is to continue measuring atmospheric trace gas (e.g., NO_2, O_3, and HCHO) from the ozone monitoring instrument (OMI) (Levelt et al., 2006), which is still operating after its launch in July 2004 (Veefkind et al., 2012). Like OMI, the TROPOMI satellite crosses the equator in a sun-synchronous polar orbit at approximately 13:30 local time with near-UV visible (270 to 500 nm) spectrometers. It has almost global daily coverage and a wavelength window from 405 to 465 nm. The ground pixel size of the TROPOMI data is

https://doi.org/10.5194/egusphere-2025-2687
Preprint. Discussion started: 27 August 2025

7 km × 3.5 km (5.5 km × 3.5 km after 6 August 2019). It has a higher spatial resolution than previous instruments, a signal-to-noise ratio improvement of approximately 1 to 5 times, and a slant-column density error for individual pixels 30% lower than that for OMI retrievals (20% after 6 August 2019). The TROPOMI data has been well validated and used for top-down emission estimates (Vigouroux et al., 2020).

TROPOMI S-5P level 2 data products for NO_2 and HCHO from June to September 2019 were used in this study. Retrievals with quality assurance values greater than 0.7 were extracted and regridded to a resolution of 0.1° × 0.1° in molec./cm^2, and remapped to matching the modeling grids (units converted to 10^{15} molec./cm^2).

2.2 Model settings

The CAMx model version 7.10 (ENVIRON, 2021) was used in this study. The model master grid (36 × 36 km) covered all provinces of China with longitudes of 57°E−161°E and latitudes of 1°N–59°N, with 20 vertical layers and the top height of approximately 20 km, and contained grids of 200 columns × 160 rows (**Fig. 1**). The meteorological data used for the simulations were obtained from the Weather Research and Forecast (WRF) v3.9.1.1 model (Skamarock et al., 2019). The modeled meteorological parameters were verified and demonstrated in the **Supplementary Note 3**. The chemical mechanism, SAPRC07 was chosen for the gas phase chemistry. Photolysis rates used in the CAMx model were calculated using O_3 column data from OMI.

The emission inventory of China integrating CO_2 with air pollutants, as reported by Zhi et al. (2024) was chosen as the base emission inventory in this study. The emission data used outside of China was from the Regional Emission inventory in Asia, version 2.1 (REAS2.1; Kurokawa en Ohara, 2019). The Sparse Matrix Operator Kernel Emissions (SMOKE) was used to facilitate the allocation of emissions by sector and the categorization of VOCs and particulate matter. The emissions from natural sources were modeled by the Model of Emissions of Gases and Aerosols from Nature (MEGAN) v3.1. (Guenther et al., 2019).

https://doi.org/10.5194/egusphere-2025-2687
Preprint. Discussion started: 27 August 2025

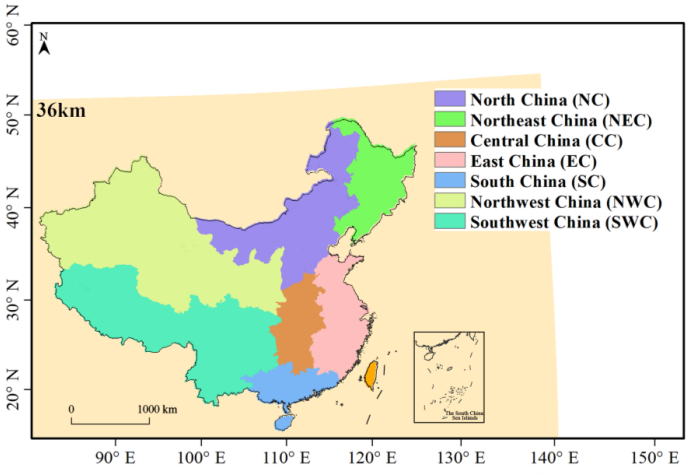

Figure 1: 36 km × 36 km domain for the CAMx simulation (different regions shown in various colours).

High-order DDM (Hakami et al., 2005) is a widely used method for the forward sensitivity analysis, and was used in this study to simulate changes in O_3 concentrations due to NO_x and VOCs emission perturbations. This method effectively calculated semi-normalized sensitivity coefficients by solving sensitivity equations and the model equations simultaneously. It also has been used as one of the key methods for preparing emission reduction plans and state air quality implementation plans (Liao and Hou, 2015). The sensitivity factor S_{ij}^{*} is defined as

$$S_{ij}^{*} = S_{i,j}^{(1)} + S_{ij}^{(2)} = P_{i,j}\frac{\partial C}{\partial p_{i,j}} + P_i\frac{\partial}{\partial p_i}\left(P_j\frac{\partial C}{\partial p_j}\right) =$$

$$P_{i,j}\frac{\partial C}{\partial(\epsilon_{i,j}P_{i,j})} + P_i\frac{\partial}{\partial\epsilon_i P_i}\left(P_j\frac{\partial C}{\partial\epsilon_j P_j}\right) = \frac{C}{\partial\epsilon_{i,j}} + \frac{\partial^2 C}{\partial\epsilon_i\partial\epsilon_j} \quad (1)$$

where i and j are air pollutant types, $S_{i,j}^{(1)}$ and $S_{i,j}^{(2)}$ are the semi-normalized first- and second-order sensitivity coefficients, C is the pollutant concentration, $P_{i,j}$ is the sensitivity parameter in the base case, $p_{i,j}$ is the base value of source emissions, and $\epsilon_{i,j}$ is the perturbation ratio (between 0 and 1).

2.3 Inverse modeling

2.3.1 Discrete Kalman filter

The Kalman filter theory developed by Kalman (1960) has been widely used from as early as 1983 when Cunnold et al. (1994) applied the Kalman filter to a 2D model to predict the atmospheric lifetime of freon-11 ($CFCl_3$). Haas - Laursen et al. (1996) then compared and tested various correction methods for the Kalman filter, showing that the adaptive iterative

https://doi.org/10.5194/egusphere-2025-2687
Preprint. Discussion started: 27 August 2025

approach gave the most accurate simulation results. Following that, a DKF using discrete recursive optimal linear filtering was conducted, directly using the sensitivities of pollutant concentrations to emissions to calculate the nonlinear relation between pollutants and sources through a multiple iteration algorithm (Gilliland and Abbitt, 2001; Prinn, 2013). Using the DKF method combined with satellite observations to derive top-down air pollutant emission inventories and to calculate their possible biases, has recently been performed (Napelenok et al., 2008; Tang et al., 2013). The DKF method is described as

$$\bar{E}_{i+1} = \bar{E}_i + G_i\left(\bar{C}_i^{obs} - \bar{C}_i^{mod}\right) \quad (2)$$

$$G_i = \mathrm{A}_i S_i^T (S_i \mathrm{A}_i S_i^T + \mathrm{R}_i)^{-1} \quad (3)$$

$$\mathrm{A}_{i+1} = \mathrm{A}_i - G_i S_i \mathrm{A}_i \quad (4)$$

where $\bar{E}_{i+1}$ is the updated emission regulator, $\bar{E}_i$ is the emission regulator at the time of the baseline simulation scenario, A_{i+1} is the updated emission-related covariance, A_i is the covariance on emissions at the time of the baseline simulation scenario, $\bar{C}^{obs}$ and $\bar{C}^{mod}$ are the observed (satellite data or station monitoring data) and modelled concentrations of an air pollutant respectively, the calculated G_i is the Kalman gain, S_i is the sensitivity of the pollutant to emissions at the time of the baseline simulation scenario, and R_i is the covariance of the observed data. Combining the equations gives

$$\bar{E}_{i+1} = \bar{E}_i + \mathrm{A}_i S_i^T (\mathrm{S}_i \mathrm{A}_i S_i^T + \mathrm{R}_i)^{-1}\left(\bar{C}_i^{obs} - \bar{C}_i^{mod} - \mathrm{S}_i \bar{E}_i\right) \quad (5)$$

At observation correction step time step *i*, the inversion process corrects the predicted emissions ($\bar{E}_i$) and the predicted emission covariance (A_i) by taking the observations ($\bar{C}^{obs}$) and inverts them to obtain the Kalman gain (G_i), then generates the corrected emissions ($\bar{E}_{i+1}$) and the corrected emission covariance (A_{i+1}). The iteration stops when the regulation parameter is extremely close to the present value ($\frac{\bar{E}_{i+1}-\bar{E}_i}{\bar{E}_i} < 0.01$).

2.3.2 Joint inversion for NO_x and VOC emissions

Joint inversion considers multiple pollutants within a matrix framework, involving cross-sensitivity coefficients ($S_{i,j}^{(2)}$) and incorporating both simulated ($\bar{C}_i^{mod}$) and observed ($\bar{C}_i^{obs}$) pollutant concentrations, as detailed in **Eq. (6) to Eq. (8)**. The variables in **Eq. (5)** update as follows:

$$\bar{E}_{i+1} = \bar{E}_i + A_i S_{matrix}^T \left(S_{matrix} A_i S_{matrix}^T + R_i\right)^{-1} (\bar{C}_{matrix}^{obs} - \bar{C}_{matrix}^{mod} - S_{matrix} \bar{E}_i) \quad (6)$$

The detailed variables in **Eq. (6)** are as follows:

https://doi.org/10.5194/egusphere-2025-2687
Preprint. Discussion started: 27 August 2025

$$S_{matrix} = \begin{bmatrix} S_{NOx}^{NO2^{(1,1)}} & S_{VOC}^{NO2^{(1,1)}} \\ S_{NOx}^{NO2^{(1,2)}} & S_{VOC}^{NO2^{(1,2)}} \\ \vdots & \vdots \\ S_{NOx}^{HCHO^{(1,1)}} & S_{VOC}^{HCHO^{(1,1)}} \\ S_{NOx}^{HCHO^{(1,2)}} & S_{VOC}^{HCHO^{(1,1)}} \\ \vdots & \vdots \end{bmatrix} \quad (7)$$

$$C_{matrix} = \begin{bmatrix} NO2^{(1,1)} \\ NO2^{(1,1)} \\ \vdots \\ HCHO^{(1,1)} \\ HCHO^{(1,1)} \\ \vdots \end{bmatrix} \quad (8)$$

In S_{matrix} we considered the sensitivity of NO_2 and HCHO concentrations to NO_x and VOC emissions $S_{NOx}^{NO2^{(1,1)}}$ and $S_{VOC}^{HCHO^{(1,1)}}$ and the sensitivity of NO_2 concentrations to VOC emissions $S_{VOC}^{NO2^{(1,1)}}$ and HCHO concentrations to NO_x emissions $S_{NOx}^{HCHO^{(1,1)}}$. In **Eq. (7)** and **Eq. (8)**, (1,1) in the upper right corner indicates the first row and first column of the simulation grid. The joint inversion approach considered not only the nonlinear chemical feedbacks between NO_2 concentration and NO_x emission and HCHO concentrations and VOCs emissions, respectively, but also the mutual influence between NO_2 concentration and VOCs emission and HCHO concentration and NO_x emission, respectively.

The emission-related covariance matrix A_i for the baseline simulation scenario followed a reference setting (H. Souri et al., 2020), with a set of a priori error of 50% for NO_x emissions, σ_i^{ENOx}, 150% for VOCs emissions, σ_i^{EVOC}, and $A_i = \sigma_i^{E^2}$. An important assumption of the inversion methodology is that inconsistencies between satellite observations and model outputs arise mainly from emission inventories. Whereas the observed data covariance R_i can also introduce other errors, it ultimately limits only the extent to which the final inversion results are close to the observed values. The error σ_i^{obs} in the satellite data product includes instrumental errors and other uncertainties that were difficult to quantify. In this study, to prevent data instability, $R_i = Max\left[\sigma_{min}^{obs}, \bar{C}_{matrix}^{obs} \times \chi^{obs}\right]^2$, with σ_{min}^{obs} being a minimum value of 0.8×10^{15} molec./cm^2 and 1.0×10^{15} molec./cm^2 for the TROPOMI NO_2 and HCHO column concentration, respectively. χ^{obs} represents the satellite data uncertainty and was set to 35% for NO_2 and 20% for HCHO column concentrations, respectively. It assumed that both covariance matrices were diagonal matrices. Since the satellite data used in this study were monthly averages, the correction factors were also monthly averages for each month from June to September 2019.

2.3.3 Pseudodata test

Before formally inverting the emission inventory with satellite data, a pseudodata test was performed to evaluate the effectiveness of the inversion approach and to ensure that the joint inversion was accurate within the study area. To determine the inversion performance more quickly for a given change in emissions, the pseudodata test was randomly

https://doi.org/10.5194/egusphere-2025-2687
Preprint. Discussion started: 27 August 2025

selected for 10 days (July 1st to July10th) with the first 3 days as the model start-up and excluded from the calculation. The principle of the pseudodata test was to add a known perturbation to the existing inventory, and the perturbation values for the test varied randomly from 0.5 to 1.6 (**Table S1**). The simulated concentrations in the baseline scenario were used as observed concentrations to invert the perturbed inventory, testing whether the inversion could restore the perturbed inventory to its original values.

As previously mentioned, the pseudodata test also required the emission-related covariance matrix A_i and the observed data covariance R_i. The a priori errors σ_i^{ENOx} and σ_i^{EVOC} for all source regions were assumed to be consistent with the formal inversion, setting at 50% and 150% respectively. The observed data covariance R_i was determined in the formal inversion based on the uncertainty of the satellite data product. However, in the pseudodata test, the inversion was used the simulated concentrations as the observed concentrations, and the overall process was fully controllable. Hence, χ^{obs} was therefore set to 0, and the σ_{min}^{obs} for the simulated NO_2 and HCHO column concentrations were set to match the formal inversion at 0.8×10^{15} molecules·cm^{-2} and 1×10^{15} molecules·cm^{-2} respectively.

The pseudodata test results for different regions showed in **Fig. 2**. The inversion approach successfully and simultaneously reset the NO_x and VOCs emissions from the baseline scenario for each region within a few iterations. The corresponding NO_2 and HCHO column concentrations were well reproduced, and the inversion converged closely to the original emission adjustment factors, indicating that the inversion approach was feasible for this study (**Fig. S1**).

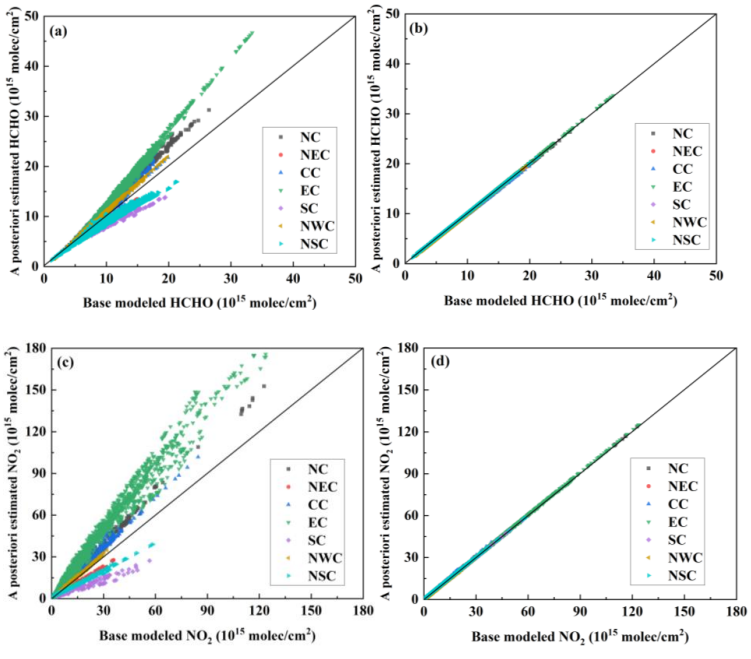

https://doi.org/10.5194/egusphere-2025-2687
Preprint. Discussion started: 27 August 2025

Figure 2: Pseudodata analysis for region-based DKF inversion for HCHO (top) and NO_2 (bottom) column concentrations

3. Results

3.1 Comparisons of emission changes under satellite data constraints

A quantitative analysis of NO_x and VOCs emissions was conducted in different regions in China to assess the effects of inversions on emission estimates (**Table 1**). The trends in NO_x emissions varied across regions. In the North China (NC) region, the NO_x emissions decreased from a prior estimate of 622 tons to 428 tons after joint inversion (a reduction of 31.2%) and further to 412 tons after individual inversion (a reduction of 33.8%). However, in the Central China (CC) region, despite the decrease in NO_x emissions to 462 tons after individual inversion (a reduction of 34.5%), the emissions increased to 1,029 tons after joint inversion (an increase of 45.9%), indicating that interaction between NO_x and VOCs in the inversion may lead to various estimates of emissions. In terms of VOCs emissions, the regional inversion produced diverse results as well. In the NC region, the VOCs emissions slightly increased after joint inversion (787 tons, an increase of 13.6%) but surged to 1,231 tons via individual inversion (an increase of 77.6%), which might have stemmed from the diversity and complexity of VOCs emission sources. Overall, significant variations observed in both inversed NO_x and VOC emission estimates in different regions under different inversion approaches. The inversed NO_x emissions over China decreased from a priori by 39% and 17% via individual and joint inversions, respectively, and the inversed VOCs emissions over China increased from a priori by 45% and 55% via individual and joint inversions, respectively.

Table 1. A priori and a posteriori NO_x and VOCs emissions in different regions in China

Region	NO_x emissions			VOCs emissions		
	Posteriori (joint)	Posteriori (individual)	Priori	Posteriori (joint)	Posteriori (individual)	Priori
NC	428	412	622	787	1,231	693
CC	1,029	462	705	2,604	1,465	1,099
EC	1,408	846	1,172	4,634	3,929	3,059
SC	613	405	619	1,516	1,473	962
NWC	740	770	1,776	654	1,250	606
SWC	899	755	1,382	1,295	1,301	960
NEC	847	722	937	1,573	1,521	1,021

Spatial distribution analysis of VOCs emissions (**Fig.3**) showed that a priori VOCs emissions were concentrated predominantly in densely populated areas such as the Beijing–Tianjin–Hebei (BTH) and its surrounding areas, the Yangtze River delta (YRD), and the Pearl River delta (PRD). VOCs emissions in NC and EC regions increased substantially after individual inversion. Urban VOCs emissions in CC and Eastern China (EC) significantly increased via joint inversion.

https://doi.org/10.5194/egusphere-2025-2687
Preprint. Discussion started: 27 August 2025

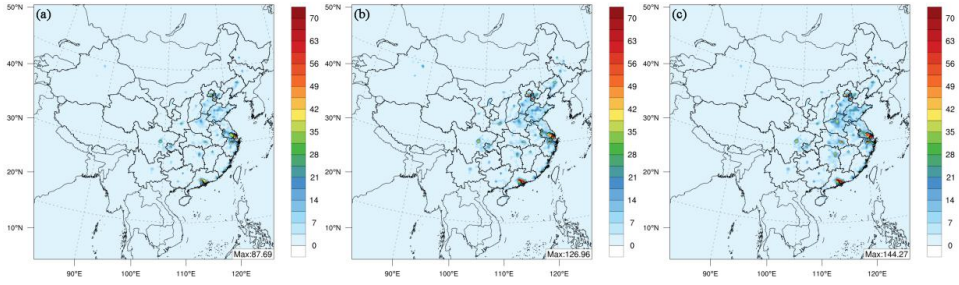

Figure 3. Spatial distribution of (a) a priori, (b) individual inversed, and (c) joint inversed VOCs emissions with TROPOMI constraints

In contrast, the spatial distribution of a priori NO_x emissions was more dispersed than that of VOCs emissions (**Fig.4**). There was a marked decrease in China's total NO_x emissions after individual inversion, while joint inversion has led a reduction of NO_x emissions mostly in Western China.

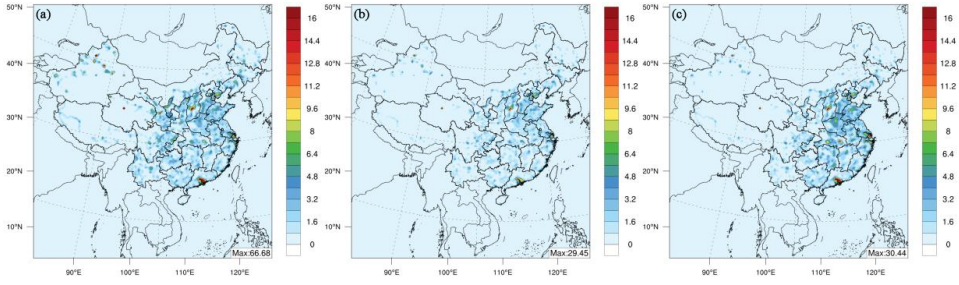

Figure 4. Spatial distributions of (a) a priori, (b) individual inversed, and (c) joint inversed NO_x emissions with TROPOMI constraints

3.2 Effects of inversed emissions on column concentrations

A comprehensive analysis of the NO_2 and HCHO column concentrations in China was conducted. The modeled results of a priori emissions, individual inversed emissions, and joint inversed emissions were compared with the TROPOMI satellite data to assess the effects of different inversion approaches on column concentrations. The spatial distribution of NO_2 column concentrations (**Fig. 5**) showed that modeled results by the a priori emissions significantly overestimated NO_2 levels across central, eastern and northwestern China, with regional maxima up to twice the values observed by TROPOMI. In contrast, the NO_2 column concentrations obtained through joint inversion showed a spatial distribution more consistent with TROPOMI, aligning with the range of observed concentrations and stabilizing at a maximum of approximately 15molec./cm^2. However, there were slight overestimations persisted in Henan and Shandong Province, possibly due to the application of uniform emission adjustment coefficients in urban areas of the CC and EC regions. On the other hand, a

https://doi.org/10.5194/egusphere-2025-2687
Preprint. Discussion started: 27 August 2025

marked reduction in NO_2 column concentrations across China was led by the individual inversion, particularly pronounced in the BTH and the YRD regions.

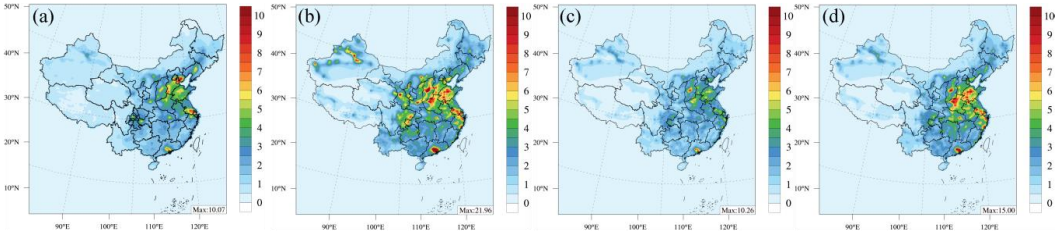

Figure 5. Spatial distribution of tropospheric NO_2 column concentrations from (a) TROPOMI satellite data, (b) a priori emissions simulation, (c) individual inversed emissions simulation (d) joint inversed emissions simulation for June to September 2019

The spatial distribution of the HCHO column concentrations (**Fig. 6**) showed that the HCHO levels observed by TROPOMI in central EC were considerably higher than those predicted by the a priori emissions, with most areas exceeding 15molec./cm^2, whereas the simulated values generally fell below 12molec./cm^2. The simulated HCHO column concentrations were significantly increased by both individual and joint inversions, with the maximum value reaching approximately 19molec./cm^2 after individual inversion, closely matching the peak values from TROPOMI. However, a tendency towards underestimation remained across the overall distribution. Notably, the HCHO column concentrations in NC, CC, and EC regions yielded by the joint inversion closely resembled the satellite data, successfully capturing the belt-like distribution characteristic of the TROPOMI HCHO column. Although both individual and joint inversions have improved the a priori emission estimates, joint inversions have demonstrated a superior alignment with the TROPOMI observations.

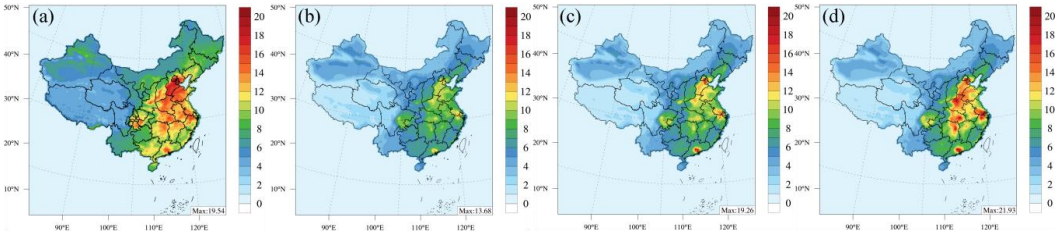

Figure 6. Spatial distribution of tropospheric HCHO column concentrations from (a) TROPOMI satellite data, (b) a priori emissions simulation, (c) individual inversed emissions simulation (d) joint inversed emissions simulation for June to September 2019

https://doi.org/10.5194/egusphere-2025-2687
Preprint. Discussion started: 27 August 2025

3.3 Effects of inversed emissions on ground-level concentrations

The inverse modeling adjusted NO_x and VOCs emissions to bring simulated tropospheric NO_2 and HCHO column concentrations closer to the TROPOMI satellite retrievals. To verify the accuracy of the inversed emission inventory and its performance on ground-level O_3 simulations, ground-monitoring data was used to validate the model outputs. A priori and a posteriori emissions-based simulations of ground-level O_3 concentrations were compared with observed data (**Fig.7**, NO_2 comparisons are in **Supplementary Note 4**). The joint inversed emission-based simulation significantly improved the modeled surface O_3 concentrations across China (**Fig. 7**), particularly in the NEC and CC regions, where a priori and individual inversed-based emission simulations substantially underestimated O_3 concentrations. The model performance of O_3 simulation in the NWC region improved insignificantly, possibly because the spatial distribution of emissions in the NWC region were concentrated in certain areas, while the adjustments were applied for the entire region.

The model performance statistics were shown in **Table 2**. The correlation coefficient (R) is generally high for both a priori and a posteriori emissions-based simulations. (More statistical results are in **Figs. S10 and S11**.). In most regions, the joint inversion outperformed the individual inversion and a priori simulation in terms of normalized mean bias (NMB) and normalized mean error (NME). Especially in the EC region, the joint inversion achieved NMB and NME values of 0.5% and 8.7%, respectively, significantly lower than the other two simulations, demonstrating the effectiveness of the joint inversion in reducing model bias and error. Moreover, the joint inversion simulation also showed significant reductions in mean bias (MB) and mean error (ME), indicating that the model predictions were very close to the actual observations. The joint inversion simulation had lower root mean square error (RMSE) than that of the individual inversion and a priori simulation in most regions, showing better performance in improving model accuracy. The observation mean and the model mean served as an indicator for the model predictive precision. In various regions, the model mean derived from the joint inversion approach had a closer correspondence to the observation mean, particularly pronounced in the NC, EC, and SC regions of China, thereby reinforcing the advantage of the joint inversion approach in improving the model performance.

https://doi.org/10.5194/egusphere-2025-2687
Preprint. Discussion started: 27 August 2025

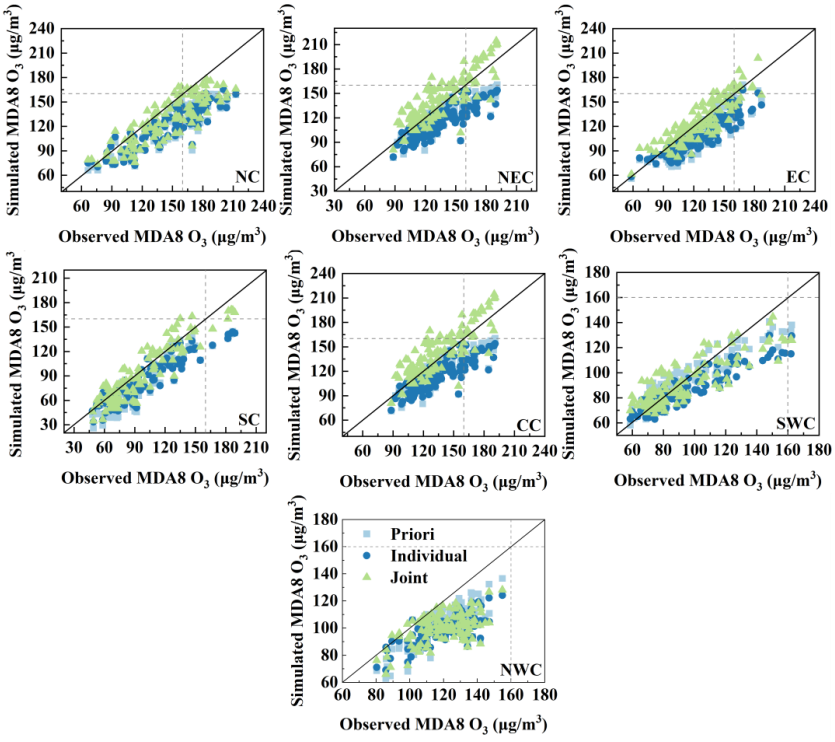

276
277 **Figure 7. Simulated ground-level MDA8 O_3 concentrations by a priori, individual inversed, and joint inversed emissions against**
278 **the ground monitored data at different regions in China**

https://doi.org/10.5194/egusphere-2025-2687
Preprint. Discussion started: 27 August 2025

Table 2. Model performance of simulated MDA8 O_3 concentrations against observations in different regions in China. (*R* – correlation, NMB – normalized absolute bias, NME – normalized absolute error, MB – mean bias, ME – mean error, RMSE – root mean square error, Obs. – observation mean, Mod. – model mean)

		R	NMB (%)	NME (%)	MB (μg/m^3)	ME (μg/m^3)	RMSE (μg/m^3)	Obs. (μg/m^3)	Mod. (μg/m^3)
Individual		0.79	-12.9	15.4	-13.2	15.6	19.5	100	87
Joint	NEC	0.79	-9.9	13.7	-10.2	14.0	17.8	100	90
a Priori		0.79	-13.9	15.6	-14.0	15.8	20.0	100	86
Individual		0.88	-17.7	18.3	-26.4	27.1	29.6	146	119
Joint	NC	0.86	-10.4	12.8	-16.3	19.4	22.3	146	129
a Priori		0.87	-17.9	18.0	-26.6	26.7	29.4	146	119
Individual		0.90	-13.9	14.3	-17.8	18.4	20.9	128	110
Joint	EC	0.89	0.5	8.7	0.2	11.0	13.3	128	128
a Priori		0.90	-13.5	13.9	-17.5	18.0	20.8	128	110
Individual		0.86	-15.8	16.8	-15.2	16.2	20.2	99	83
Joint	SC	0.86	-4.7	12.3	-3.7	11.6	14.2	99	95
a Priori		0.86	-17.9	18.4	-16.9	17.5	21.4	99	82
Individual		0.89	-15.4	15.5	-20.9	21.1	24.5	136	115
Joint	CC	0.89	5.9	10.7	8.0	14.5	17.3	136	144
a Priori		0.89	-12.7	13.0	-17.5	17.8	21.4	136	118
Individual		0.75	-17.1	17.2	-21.0	21.1	22.7	120	99
Joint	NWC	0.67	-15.6	15.9	-19.3	19.6	21.8	120	100
a Priori		0.77	-14.9	14.9	-18.1	18.2	20.2	120	102
Individual		0.93	-8.8	11.9	-9.0	11.6	14.6	94	85
Joint	SWC	0.90	-0.4	12.2	-1.1	11.3	14.4	94	93
a Priori		0.93	-1.4	9.0	-1.9	8.5	10.4	94	92

3.4 Effects of inversed emissions on O_3 sensitivities

To explore the effect of different inversion approaches on the O_3 sensitivities, the spatial distributions of the O_3 formation regimes derived from OMI satellite data and various inversion approach simulations were analysed for June to September 2019 (**Fig. 8**). OMI satellite-based O_3 sensitivity showed that most regions in China are predominantly NO_x-limited for O_3 formation during the summer, with VOC-limited or transitional regime present in some key areas such as BTH, YRD, and PRD. This pattern is consistent with the findings from Wang et al. 2023.

In addition, the a priori emission simulation results shown in **Fig. 8b** illustrated a broader range of transitional regimes in NC and EC, especially in key areas such as BTH, YRD, and PRD, which was more extensive compared to those demonstrated by the satellite-based results in **Fig. 8a**. However, O_3 sensitivities simulated by the individual inversed (**Fig. 8c**) and the joint inversed (**Fig. 8d**) emissions showed significant differences compared to that from a priori emission simulation. Although some systematic noise in the central region of China were observed in both inversion simulations, the sensitivities indicated that most regions in China had shifted to NO_x-limited regimes.

https://doi.org/10.5194/egusphere-2025-2687
Preprint. Discussion started: 27 August 2025

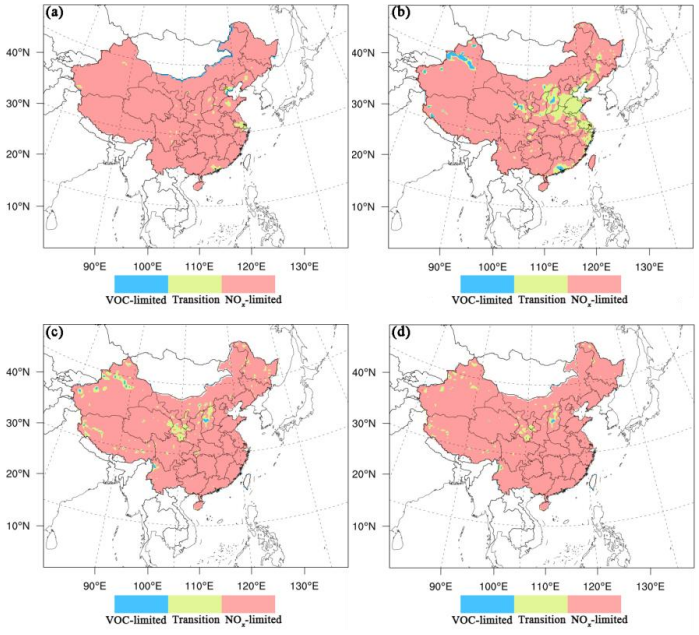

Figure 8. Spatial distributions of O_3 sensitivities from (a) satellite data-derived, (b) a priori emissions, (c) individual inversed emissions, and (d) joint inversed emissions simulations for June–September 2019

4. Conclusion and discussion

The findings of this study offered critical insights into the effects of inversion approaches on the top-down NO_x and VOCs emission estimates, and the consequential influences on O_3 sensitivity simulations in China. The analysis emphasized the significant regional variability in the a priori and a posteriori emission estimates, with the NC region demonstrating a substantial reduction in NO_x emissions, reaching 31.2% after joint inversion and further to 33.8% following individual inversion. However, contrasting results were observed in the CC region, where the joint inversion increased NO_x emissions by 45.9%, while the individual inversion decreased NO_x emissions by 34.4%. Although the NC region was observed a slight increase of VOCs emissions after the joint inversion, individual inversion led to a significant boost of VOCs emission estimates, indicating that various estimates of emissions may resulted in different inversion approaches, and the mutual influence of NO_x and VOCs cannot be neglected in the inversion process.

Overall, the inversion brought down NO_x emissions over China by approximately 30% and brought up VOCs emissions over China by around 50%. This NO_x reduction trend aligns with prior multi-species inversion studies, which consistently report decreasing NO_x emissions over eastern China (Qu et al., 2017; Souri et al., 2020; Wang et al., 2020). Satellite-

https://doi.org/10.5194/egusphere-2025-2687
Preprint. Discussion started: 27 August 2025

constrained inversions, including ours, show steeper declines than a priori inventories, especially in industrial hotspots like the North China Plain (NCP) and Yangtze River Delta. Notably, Wang et al. (2020) documented smaller national decreases (5.8%–6.5%) but similarly large localized drops (up to 40% in the NCP). Discrepancies emerge in central and western China: while our results show local NO_x increases, Wang et al. (2020) reported 3%–8% decreases, potentially due to differences in a priori inventories or satellite data limitations (Qu et al., 2022). For VOCs, our inferred ~50% national increase is consistent with evidence of widespread underestimation in East Asia. Souri et al. (2020) found a 25% post-inversion rise in the NCP, and Choi et al. (2022) reported a 47% total increase using hybrid inversion methods, supporting the robustness of VOCs underestimation.

The joint inversion simulation generally outperformed that of individual inversion in reducing model bias and error and improving the correlation coefficients between model predictions and observations. In EC, the joint inversion simulation achieved a NMB of 0.5% and a NME of 8.7% compared to the observed data, which were significantly lower than those of the individual inversion and a prior emission-based simulations. In addition, the joint inversion approach had a closer alignment with TROPOMI-observed NO_2 and HCHO column concentrations, effectively capturing the the belt-like distribution of HCHO, and with a stabilized maximum column concentration of approximately 15molec./cm² for NO_2. The model performance of ground-level O_3 concentration simulations were significantly enhanced by the joint inversion approach, especially in the regions like NEC and CC, where a priori emission-based simulations significantly underestimated O_3 levels. Furthermore, the O_3 formation regimes over China predominantly shifted towards NO_x-limited conditions during the summer using inversed emissions.

Notwithstanding these findings, several limitations warrant consideration: (1) Satellite data uncertainties (coarse resolution masking urban sources; monthly TROPOMI averaging obscuring short-term variability) coupled with inversion sensitivity constraints; (2) Chemical interference (e.g., NH_3 uncertainty propagating NO_x errors via nitrate chemistry); (3) Temporal and spatial mismatches in a priori inventory leading to biased adjustments; (4) Targeting total VOC emissions rather than individual species may affect model simulations of secondary organic aerosols, thereby impacting inversion accuracy.

To sum up, this study emphasized the critical role of inversion approaches in refining emission estimates and enhancing the accuracy of atmospheric models. Although the joint DKF inversion approach appears to offer several advantages over individual DKF inversion, it is crucial to continue exploring and refining these methods to address the remaining uncertainties and improve our understanding of air pollution dynamics. Furthermore, we quantitatively assess the causal impacts of these emission adjustments on regional O_3 sensitivity regime transitions. Future research could focus on integrating various observational data sources into the inversion process, such as satellite data, ground-based and aircraft

https://doi.org/10.5194/egusphere-2025-2687
Preprint. Discussion started: 27 August 2025

measurements, to further enhance the accuracy and reliability of inversion-derived emission estimates and their implications for air quality management and policy-making.

Acknowledgments

This work was supported by the Jing-Jin-Ji Regional Integrated Environmental Improvement-National Science and Technology Major Project (Nos. 2024ZD1200502), the Basic Scientific Research Business Expense Project of Central-level Public Welfare Scientific Research Institutes (Nos. 2024YSKY-08) and the Major Science and Technology Project of the Xinjiang Uygur Autonomous Region—Research on the Comprehensive Causes and Advanced Control Technologies for Severe Air Pollution in the Urumqi-Changji-Shihezi Region (Nos. 2024A03012-2).

Code/Data availability

The data used in this study are available from the corresponding author upon request (tangwei@craes.org.cn).

Author contribution

XD and WT designed the research, analyzed data, and prepared the manuscript. CY provided TROPOMI HCHO and NO_2 satellite data. JH provided data modification suggestions. ZZ performed meteorological simulations. YY performed air quality model calculations. YL provided emission inventory calculations. MC and FM commented on the manuscript.

Competing interests

The authors declare that they have no conflict of interest.

References

Choi, J., Henze, D. K., Cao, H., Nowlan, C. R., González Abad, G., Kwon, H., Lee, H., Oak, Y. J., Park, R. J., Bates, K. H., Maasakkers, J. D., Wisthaler, A., and Weinheimer, A. J.: An Inversion Framework for Optimizing Non-Methane VOC Emissions Using Remote Sensing and Airborne Observations in Northeast Asia During the KORUS-AQ Field Campaign, J. Geophys. Res. Atmos., 127, 1–27, https://doi.org/10.1029/2021jd035844, 2022.

Cunnold, D. M., Fraser, P. J., Weiss, R. F., Prinn, R. G., Simmonds, P. G., Miller, B. R., Alyea, F. N., and Crawford, A. J.: Global trends and annual releases of CCl3F and CCl2F2 estimated from ALE/GAGE and other measurements from July 1978 to June 1991, J. Geophys. Res. Atmos., 99, 1107–1126, 1994.

ENVIRON, R.: User's Guide Comprehensive Air Quality Model with Extensions version 7.10, in, ENVIRON Intl, 2021.

Gerbig, C., Lin, J. C., Wofsy, S. C., Daube, B. C., Andrews, A. E., Stephens, B. B., Bakwin, P. S., and Grainger, C. A.: Toward constraining regional-scale fluxes of CO_2 with atmospheric observations over a continent: 2. Analysis of COBRA data using a receptor-oriented framework, J. Geophys. Res. Atmos., 108, https://doi.org/https://doi.org/10.1029/2003JD003770, 2003.

https://doi.org/10.5194/egusphere-2025-2687
Preprint. Discussion started: 27 August 2025

Gilliland, A. and Abbitt, P. J.: A sensitivity study of the discrete Kalman filter (DKF) to initial condition discrepancies, J. Geophys. Res. Atmos., 106, 17939–17952, 2001.

Guenther, A., Jiang, X., Shah, T., Huang, L., Kemball-Cook, S., and Yarwood, G.: Model of emissions of gases and aerosol from nature version 3 (MEGAN3), Air Pollut. Model. its Appl. XXVI. Springer, Cham, 187, 2019.

H. Souri, A., R. Nowlan, C., González Abad, G., Zhu, L., R. Blake, D., Fried, A., J. Weinheimer, A., Wisthaler, A., Woo, J. H., Zhang, Q., E. Chan Miller, C., Liu, X., and Chance, K.: An inversion of NO_x and non-methane volatile organic compound (NMVOC) emissions using satellite observations during the KORUS-AQ campaign and implications for surface ozone over East Asia, Atmos. Chem. Phys., 20, 9837–9854, https://doi.org/10.5194/acp-20-9837-2020, 2020.

Haas-Laursen, D. E., Hartley, D. E., and Prinn, R. G.: Optimizing an inverse method to deduce time-varying emissions of trace gases, J. Geophys. Res. Atmos., 101, 22823–22831, 1996.

Hakami, A., Henze, D. K., Seinfeld, J. H., Chai, T., Tang, Y., Carmichael, G. R., and Sandu, A.: Adjoint inverse modeling of black carbon during the Asian Pacific Regional Aerosol Characterization Experiment, J. Geophys. Res. D Atmos., 110, 1–17, https://doi.org/10.1029/2004JD005671, 2005.

Jiang, J., Aksoyoglu, S., Ciarelli, G., Baltensperger, U., and Prévt, A. S. H.: Changes in ozone and $PM_{2.5}$ in Europe during the period of 1990–2030: Role of reductions in land and ship emissions, Sci. Total Environ., 741, 140467, 2020.

Jung, J., Choi, Y., Souri, A. H., Mousavinezhad, S., Sayeed, A., and Lee, K.: The Impact of Springtime-Transported Air Pollutants on Local Air Quality With Satellite-Constrained NO_x Emission Adjustments Over East Asia, J. Geophys. Res. Atmos., 127, 1–18, https://doi.org/10.1029/2021JD035251, 2022.

Kalman, R. E.: A new approach to linear filtering and prediction problems, J. Fluids Eng. Trans. ASME, 82, 35–45, https://doi.org/10.1115/1.3662552, 1960.

Khattatov, B. V, Gille, J. C., Lyjak, L. V, Brasseur, G. P., Dvortsov, V. L., Roche, A. E., and Waters, J. W.: Assimilation of photochemically active species and a case analysis of UARS data, J. Geophys. Res. Atmos., 104, 18715–18737, https://doi.org/https://doi.org/10.1029/1999JD900225, 1999.

Kurokawa, J. and Ohara, T.: Long-term historical trends in air pollutant emissions in Asia: Regional Emission inventory in ASia (REAS) version 3.1, Atmos. Chem. Phys., 1–51, https://doi.org/10.5194/acp-2019-1122, 2019.

Levelt, P. F., Van Den Oord, G. H. J., Dobber, M. R., Malkki, A., Visser, H., De Vries, J., Stammes, P., Lundell, J. O. V, and Saari, H.: The ozone monitoring instrument, IEEE Trans. Geosci. Remote Sens., 44, 1093–1101, 2006.

Li, K., Jacob, D. J., Shen, L., Lu, X., De Smedt, I., and Liao, H.: Increases in surface ozone pollution in China from 2013 to 2019: Anthropogenic and meteorological influences, Atmos. Chem. Phys., 20, 11423–11433,

https://doi.org/10.5194/egusphere-2025-2687
Preprint. Discussion started: 27 August 2025

https://doi.org/10.5194/acp-20-11423-2020, 2020.

Liao, K. J. and Hou, X.: Optimization of multipollutant air quality management strategies: A case study for five cities in the United States, J. Air Waste Manag. Assoc., 65, 732–742, https://doi.org/10.1080/10962247.2015.1014073, 2015.

Lu, B., Zhang, Z., Jiang, J., Meng, X., Liu, C., Herrmann, H., Chen, J., Xue, L., and Li, X.: Unraveling the O_3-NO_X-VOCs relationships induced by anomalous ozone in industrial regions during COVID-19 in Shanghai, Atmos. Environ., 308, 119864, https://doi.org/https://doi.org/10.1016/j.atmosenv.2023.119864, 2023.

Martin, R. V, Jacob, D. J., Chance, K., Kurosu, T. P., Palmer, P. I., and Evans, M. J.: Global inventory of nitrogen oxide emissions constrained by space-based observations of NO_2 columns, J. Geophys. Res. Atmos., 108, https://doi.org/https://doi.org/10.1029/2003JD003453, 2003.

Müller, J.-F. and Stavrakou, T.: Inversion of CO and NO_x emissions using the adjoint of the IMAGES model, Atmos. Chem. Phys., 5, 1157–1186, https://doi.org/10.5194/acp-5-1157-2005, 2005.

Napelenok, S. L., Pinder, R. W., Gilliland, A. B., and Martin, R. V.: A method for evaluating spatially-resolved NO_x emissions using Kalman filter inversion, direct sensitivities, and space-based NO_2 observations, Atmos. Chem. Phys., 8, 5603–5614, https://doi.org/10.5194/acp-8-5603-2008, 2008.

Prinn, R. G.: Measurement equation for trace chemicals in fluids and solution of its inverse, Geophys. Monogr., 2013.

Silver, B., Conibear, L., Reddington, C., Knote, C., Arnold, S., and Spracklen, D.: Pollutant emission reductions deliver decreased $PM_{2.5}$-caused mortality across China during 2015–2017, Atmos. Chem. Phys. Discuss., 2017, 1–18, https://doi.org/10.5194/acp-2019-1141, 2020.

Qu, Z., Henze, D. K., Capps, S. L., Wang, J., Keller, M., Wang, Y., and Xu, X.: Monthly top-down NO_x emissions for China (2005 – 2012): A hybrid inversion method and trend analysis, 1–26, https://doi.org/10.1002/2016JD025852, 2017.

Qu, Z., Henze, D. K., Worden, H. M., Jiang, Z., Gaubert, B., Theys, N., and Wang, W.: Sector-Based Top-Down Estimates of NOx, SO2, and CO Emissions in East Asia, Geophys. Res. Lett., 49, 1–11, https://doi.org/10.1029/2021GL096009, 2022.

Skamarock, W. C., Klemp, J. B., Dudhia, J., Gill, D. O., Zhiquan, L., Berner, J., Wang, W., Powers, J. G., Duda, M. G., Barker, D. M., and Huang, X.-Y.: A Description of the Advanced Research WRF Model Version 4, NCAR Tech. Note NCAR/TN-475+STR, 145, 2019.

Smagorjnsky, J.: The Beginnings of Numerical Weather Prediction and General Circulation Modeling: Early Recollections, in: Theory of Climate, vol. 25, edited by: Saltzman, B. B. T.-A. in G., Elsevier, 3–37,

https://doi.org/10.5194/egusphere-2025-2687
Preprint. Discussion started: 27 August 2025

https://doi.org/https://doi.org/10.1016/S0065-2687(08)60170-3, 1983.

Souri, A. H., Wang, H., González Abad, G., Liu, X., and Chance, K.: Quantifying the Impact of Excess Moisture From Transpiration From Crops on an Extreme Heat Wave Event in the Midwestern U.S.: A Top-Down Constraint From Moderate Resolution Imaging Spectroradiometer Water Vapor Retrieval, J. Geophys. Res. Atmos., 125, 1–15, https://doi.org/10.1029/2019JD031941, 2020.

Tang, W., Cohan, D. S., Lamsal, L. N., Xiao, X., and Zhou, W.: Inverse modeling of Texas NO_x emissions using space-based and ground-based NO_2 observations, Atmos. Chem. Phys., 13, 11005–11018, https://doi.org/10.5194/acp-13-11005-2013, 2013.

Trombetti, M., Thunis, P., Bessagnet, B., Clappier, A., Couvidat, F., Guevara, M., Kuenen, J., and López-Aparicio, S.: Spatial inter-comparison of Top-down emission inventories in European urban areas, Atmos. Environ., 173, 142–156, https://doi.org/10.1016/j.atmosenv.2017.10.032, 2018.

Veefkind, J. P., Aben, I., McMullan, K., Forster, H., de Vries, J. W., Otter, G., Claas, J., Eskes, H. J., de Haan, J. F., Kleipool, Q., van Weele, M., Hasekamp, O. P., Hoogeveen, R. W. M., Landgraf, J., Snel, R., Tol, P. J. J., Ingmann, P., Voors, R. H. M., Kruizinga, B., Vink, R. J. P., Visser, H., and Levelt, P. F.: TROPOMI on the ESA Sentinel-5 Precursor: A GMES mission for global observations of the atmospheric composition for climate, air quality and ozone layer applications, Remote Sens. Environ., 120, 70–83, 2012.

Vigouroux, C., Langerock, B., Aquino, C. A. B., Blumenstock, T., Cheng, Z., Mazière, M. M. De, de Smedt, I., Grutter, M., Hannigan, J. W., Jones, N. B., Kivi, R., Loyola, D. G., Lutsch, E., Mahieu, E., Makarova, M. V, Metzger, J. M., Morino, I., Murata, I., Nagahama, T., Notholt, J., Ortega, I., Palm, M., Pinardi, G., Röhling, A. N., Smale, D., Stremme, W., Strong, K., Sussmann, R., Té, Y., Roozendael, M. Van, Wang, P. C., and Winkler, H.: TROPOMI–Sentinel-5 Precursor formaldehyde validation using an extensive network of ground-based Fourier-transform infrared stations, Atmos. Meas. Tech., 13, 3751–3767, 2020.

Wang, Y., Wang, J., Zhou, M., Henze, D. K., Ge, C., and Wang, W.: Inverse modeling of SO_2 and NO_x emissions over China using multisensor satellite data - Part 2: Downscaling techniques for air quality analysis and forecasts, Atmos. Chem. Phys., 20, 6651–6670, https://doi.org/10.5194/acp-20-6651-2020, 2020.

Zhi, G., Du, J., Chen, A., Jin, W., Ying, N., Huang, Z., Xu, P., Wang, D., Ma, J., and Zhang, Y.: Progression of an emission inventory of China integrating CO2 with air pollutants: A chance to learn the influence of development on emissions, Atmos. Environ., 316, 120184, 2024.